Title
HIGH TEMPERATURE INTERNAL OXIDATION BEHAVIOR OF DILUTE Ni-Al ALLOYS

Authors
Hindam, H.
Whittle, D.P.

Publication Date
1982-04-01

LBL-14389
Preprint

Lawrence Berkeley Laboratory
UNIVERSITY OF CALIFORNIA

Materials & Molecular Research Division

Submitted to the Journal of Materials Science

HIGH TEMPERATURE INTERNAL OXIDATION BEHAVIOR OF DILUTE Ni-Al ALLOYS

H. Hindam and D.P. Whittle

April 1982

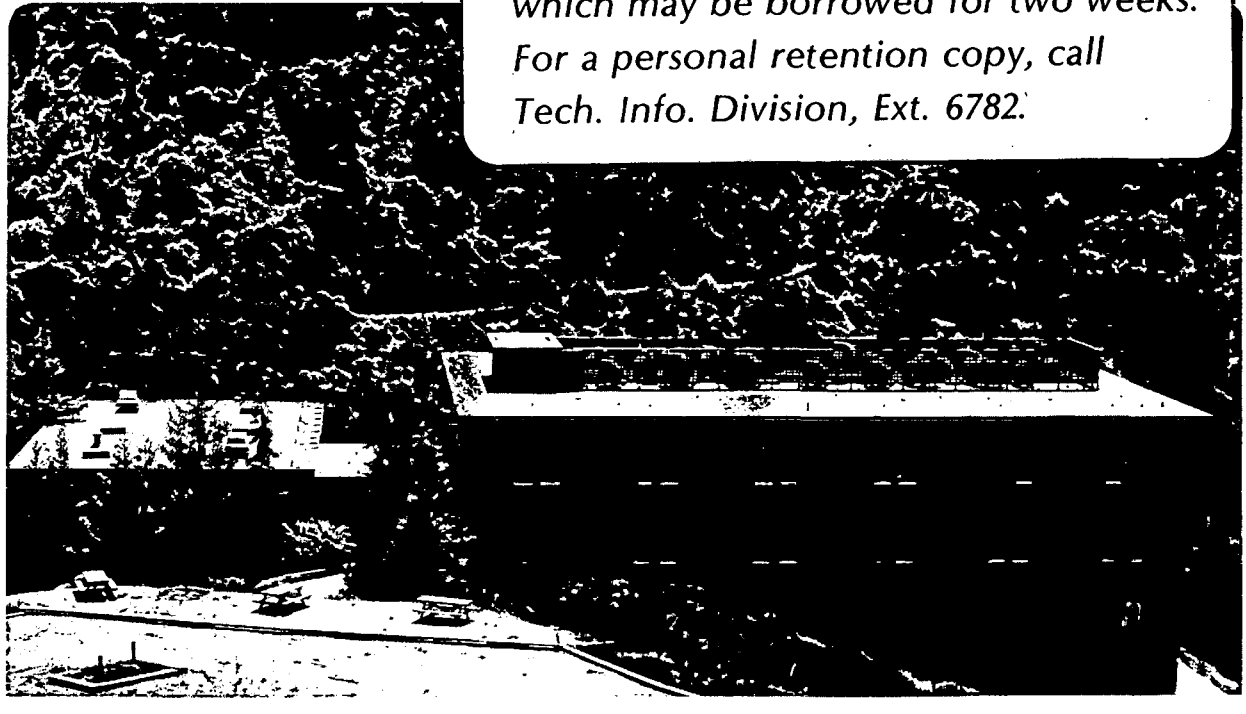

Prepared for the U.S. Department of Energy under Contract DE-AC03-76SF00098

DISCLAIMER

HIGH TEMPERATURE

INTERNAL OXIDATION BEHAVIOR OF DILUTE Ni-Al ALLOYS*[X]

H. Hindam[+] and D. P. Whittle[°]

Molecular and Materials Research Division
Lawrence Berkeley Laboratory[X]

and

[°]Department of Materials Science and Mineral Engineering
University of California
Berkeley, CA. 94720

ABSTRACT

The internal oxidation of dilute Ni-Al alloys, either pure or containing small additions of Ta or Hf, was investigated at 1200°C in air. The advance of the precipitation zone followed a parabolic relationship at a slightly decreasing rate with increasing Al content. The presence of active elements had no appreciable effect on the growth rate. The precipitate shape, size and spacing depended upon the Al concentration and more significantly on the active element additions. The morphology varied from polyhedral crystallites and epitaxial platelets in the Ni-0.5 wt.% Al alloy, to well defined cylindrical rods extending across the precipitation zone approximately normal to the reaction interface, in the alloys of higher Al content. An also continuous and similarly oriented plate-like morphology was observed in the active element-containing alloys. X-ray microanalysis indicated that the continuous precipitates consisted of $NiAl_2O_4$ and Al_2O_3. The former phase

---

*Presented at the 34th Pacific Coast Regional Meeting of the American Ceramic Society, Newport Beach, California, October 1981.

[+]Present Address: Energy, Mines and Resources Canada, Ottawa, Ontario K1A 0G1.

[X]This work was supported by the Director, Office of Energy Research, Office of Basic Energy Sciences, Materials Sciences Division of the U.S. Department of Energy under Contract No. DE-AC03-76SF00098.

comprised approximately 65 ± 5% of the outer region of the precipitation zone.

Al depletion in the alloy ahead of the precipitation front and a consequent enrichment in the form of oxide within the reaction zone inferred that growth was controlled by simultaneous outward Al and inward oxygen diffusion. No correlation was found between either the growth rate or oxygen permeability and the distribution of the precipitates. It was, therefore, concluded that the interfacial boundaries were ineffective in accelerating oxygen transport at this elevated temperature.

INTRODUCTION

The γ-NiAl solid solution phase has been the subject of several oxidation studies (1-7). At least during an incipient stage dependent upon Al content, alloys within this phase field oxidized parabolically in air or oxygen rich atmospheres forming an external duplex scale consisting of outer and inner layers of Al-doped NiO and NiO-$NiAl_2O_4$ aggregates, respectively, and an Al-depleted alloy zone containing $NiAl_2O_4/Al_2O_3$ precipitates. A previous investigation (7) suggested that the growth of the subscale was controlled by inward oxygen diffusion at a rate which was enhanced by the incoherent boundaries between the precipitates and alloy matrix. The relative contribution of the boundary transport, however, diminished rapidly with temperature in the range of 800-1100°C. The objective of the present study was to quantitatively assess the role of boundary transport, if any, at a higher temperature (1200°C), and its possible influence on the reaction mechanism by directly examining the relationship between the growth rate and morphology of the precipitate. The variation of the alloy Al content and the addition of active elements (Ta and Hf) were effective in modifying precipitate shape,

size and distribution. The present detailed microstructural observations complement those documented in a previous paper (5).

EXPERIMENTAL

Alloys of nominal compositions 0.5, 2 and 4 w/o Al were cast by electrical resistance melting of 99.99 w/o pure Ni and Al pellets in recrystallized Al_2O_3 crucibles under an ultrapure He atmosphere. The cylindrical ingots were homogeneized at 1300°C overnight in the same furnace. The Ni-2 Al ingot also served as a master alloy for preparing the active-element containing compositions. 99.999 w/o pure Hf powder and small strips sheared from a Ta foil of similar purity were used to make 1% additions to the alloy. Rectangularly shaped specimens, approximately 15x12x3 mm, were cut, metallographically polished with SiC abrasive papers down to ∿30 μm grit size and finally ultrasonically cleaned in distilled water. They were oxidized in static air at 1200°C. Layer thickness measurements were carried out on conventionally-prepared metallographic cross sections using an optical microscope. A scanning electron microscope served for detailed microstructural observations on deeply-etched specimens which were prepared by partial selective alloy dissolution in a 10 v/o Br_2-CH_3OH solution at ∿ 30°C, technique devised (5) to examine the morphology of internal precipitates.

MICROSTRUCTURE

With the exception of the Ni-4 Al alloy, as discussed later, all other compositions exhibited uniform internal oxide penetration even in the vicinity of alloy grain boundaries. However, an additional growth feature was the growth of a relatively denser population of precipitates at these alloy grain boundary locations, in the form of sheaths enveloping the alloy grains. This behavior is documented in Figure 1a-e. The close-up photographs

included as d and c, revealed the rather porous structure of these grain boundary precipitates. The latter observation in addition to uniform, unaffected penetration at the vicinity of alloy grain boundaries are confirmatory evidence that the sheaths were ineffective in impeding inward oxygen diffusion and the advance of the internal precipitation front.

Pure Alloys

Two distinct morphologies were discernible in the Ni-0.5 Al alloy (Figure 2a-d): polyhedral crystallites in preponderance to rectangular platelets (micrographs c and d). The latter particles, which were confined to the inner region of the subscale, (micrograph a) assumed defined orientations within each alloy grain (micrographs a, b and d). The relative enrichment of alloy grain boundaries with precipitates was accompanied by denudation of contiguous regions within the grains (micrograph a). This morphological feature is better illustrated in a transverse section normal to the growth direction at a triple alloy grain boundary intersection (micrograph b).

Only cylindrical, rod-like precipitates were observed in the Ni-2 Al (5) and Ni-4Al alloys. This unique morphology is documented for the latter composition in Figure 3a-d by sections along and across the precipitates. The rods extended along the precipitation zone generally normal to the reaction interfaces inferring epitaxial-free growth unlike the platelets formed in the Ni-0.5 Al alloy. The occasional coalescence of two or more rods is evident in micrograph b.

Subsequent to a relatively short initial stage of uniform penetration, discontinuous Al_2O_3 films developed randomly at the precipitation front in the Ni-4Al alloy and spread laterally to encompass the internal oxidation zone inhibiting further rod growth. The structure of this barrier film

(micrographs c and d) should be compared with the ineffective grain boundary oxide sheath, Figure 1d and e. It is evident that the former, which was not associated with alloy grain boundaries, grew laterally by precipitation of oxide in the alloy region adjoining the rods.

Active Element Containing Alloys

In contrast to the rod like precipitates formed in the pure Ni-2Al alloy, the addition of Ta or Hf led to a marked morphological change. The oxide particles in both active element containing alloys exhibited a distinct rectangular plate-like structure, Figures 4 and 5, although this was less defined in the Hf containing alloy. Similarly to the other compositions, alloy grain boundary decoration by formation of denser precipitates could be discerned (Figures 4a and 5a); nevertheless, as pointed out earlier, no evidence was found to indicate that the advance of the precipitation front was affected by the development of these localized oxide-rich regions. In fact, the precipitates can be seen to extend without any interference across the boundary sheaths (Figure 4b). As with the pure alloy, the plate-like particles grew as a continuous phase throughout the precipitation zone, perpendicular to the reaction interface. The platelets were randomly oriented throughout the alloy matrix and apparently intersected at various inclinations including merging to form large slabs (Figures 4c and d).

COMPOSITION AND PHASE DISTRIBUTION

The determination of the composition of the particles within the alloy internal oxidation zone was based on energy dispersive x-ray microanalysis. The objective was to estimate the relative amount of the $NiAl_2O_4$ and Al_2O_3 phases. To minimize interference from the substrate, the measurements were performed on deeply-etched specimens. Ni and Al K_α x-ray maps for the rod-like precipitates in the Ni-4Al alloy are included in Figure 6. The denuda-

tion of Ni and consequent enrichment of Al in the inner part of the particles adjacent to the precipitation front inferred that Al_2O_3 comprised approximately 35 ± 5% of the inner part of the subscale, whereas the rest was occupied by the spinel phase. No demarcation in the precipitate morphology was apparent at the transition 'boundary' between the two phases.

Conclusions based on these measurements were considered tentative since it was realized that the x-ray yield can be significantly influenced by structural irregularities, absorption and excitation of the underlying, essentially pure, Ni substrate. Nonetheless, deeply etched tapered sections at a small inclination with the sample surface showed a distinctive color contrast which supported the above conclusion. The spinel phase appeared as light blue whereas Al_2O_3 was light gray. The present results agreed in principle with the recent measurements of several investigators (7, 8).

As evidenced by the x-ray maps shown in Figure 7, the relative $NiAl_2O_4$/Al_2O_3 thickness was preserved in the Hf as well as Ta-containing alloys. The active elements were uniformly distributed in the subscale zone; however, no definite conclusion could be reached with respect to whether they were dissolved in the oxide or alloy matrix or existed as discrete small oxide particles.

GROWTH KINETICS

The typical overall scale morphology on the γ-NiAl solid solution alloys is illustrated in Figure 8. Since the $NiAl_2O_4$ precipitates extended in the external NiO scale forming a two-phase layer (5), the inner/outer layer interface was considered as a marker for the original alloy surface and all thickness measurements were made relative to that datum. As reported earlier, uniform internal oxide penetration was always observed, except in the Ni-4Al alloy during later stages when lateral, discontinuous Al_2O_3 films developed

at the precipitation front. In this case, only locations, where uniform penetration was still observable, were considered for evaluation of the growth kinetics. The results of these measurements are shown in Figure 9 as precipitation zone thickness, ξ versus $t^{1/2}$. The advance of the precipitation zone is thus, approximately, described by a parabolic relationship in all cases. In the pure alloys, the rate constants decreased slightly with increasing Al content. It is evident that the addition of Ta or Hf to the Ni-2Al alloy did not affect the growth rate significantly. The measured rate constants are included in Table I.

SIZE AND SPACING DISTRIBUTIONS

For selected alloy compositions, the particle size and spacing were evaluated from sections parallel to the original alloy surface where the precipitates existed as $NiAl_2O_4$. This was confirmed by the characteristic light blue color of this phase which became observable after extended deep etching. The spacing was defined as the center to center distance between nearest neighbors. The measurements, which were made at random locations, included at least 100 particles. The results are shown in Figure 10. Typical transverse sections taken at the same magnification for all alloy compositions are included in Figure 11 for a better visualization. A remarkable conspicuous difference in the distribution of the precipitates is evident. The data, included in Figure 10, were based on micrographs similar to Figure 10 but at magnifications ranging from 4K (particle spacing) to 10K (particle size).

The diameters of the rod-like precipitates in the Ni-2Al alloy showed very little variation as evidenced by the very sharp population density/size curve in Figure 10. Furthermore, the rods were well spaced apart and there was virtually no overlap between their size and spacing distributions. In

contrast, the precipitate rod diameters in the Ni-4Al alloy showed considerable spread, and this overlapped considerably with the very variable inter-rod separation. This finding, coupled with the metallographic observations discussed earlier, substantiate the impingement model which was proposed (5) to account for the transition from internal precipitation to continuous film formation in the Al-rich (Al $\gtrsim$ 4 w/o) alloys.

In the case of the Ta-containing alloy, the platelet-like precipitates were uniform in width, 0.5 μm, but there was considerable variation in their length. The latter dimension is included in Figure 10. The average particle size and spacing are given in Table I.

DISCUSSION AND CONCLUSIONS

The observed scale morphology is consistent with the thermodynamic constraints imposed by phase equilibria in the Ni-Al-O system. Indeed, a 'virtual' diffusion path can be traced on the pertinent phase diagram (9) to represent this scaling behavior (10). The Ni-rich region of an isothermal section (1000°C) is reproduced in Figure 12 on a logarithmic scale to include equilibria involving alloys with extremely small Al contents which would correspond to the composition at the reaction front upon the precipitation of Al_2O_3. The sloping lines represent the following equilibria:

$$2\underline{Al}\ (\text{alloy}) + 3/2\ O_2 = Al_2O_3(s) \qquad [1]$$

$$\underline{Ni}(\text{alloy}) + 2.54\underline{Al}(\text{alloy}) + 2.405\ O_2 = NiAl_{2.54}O_{4.81}(s) \qquad [2]$$

with $$x_{Al}\ P_{O_2}^{3/4} = \gamma_{Al}^{-1} \cdot \exp\left[\frac{\Delta G^\circ_{Al_2O_3}}{2RT}\right] \qquad [3]$$

and $$x_{Al}(1-x_{Al})^{1/2.54} \cdot P_{O_2}^{2.405/2.54} = \gamma_{Al}^{-1} \exp\left[\Delta G^\circ_{NiAl_{2.54}O_{4.81}}/2.54RT\right] \qquad [4]$$

respectively. The standard Gibbs energy of formation of the spinel phase ($NiAl_{2.54}O_{4.81}$) coexisting with NiO, was measured with respect to NiO and

Al_2O_3 (9). This was converted to a value corresponding to the above equation using $\Delta G^\circ_{Al_2O_3}$ and ΔG°_{NiO} from JANAF Thermochemical Tables (11). Assuming Henrian behavior, the activity coefficient of Al in the γ-NiAl solid solution was taken as 8×10^{-7} (12). The oxygen potentials corresponding to the invariant three phase equilibria γNiAl-$NiAl_{2.54}O_{4.81}$-Al_2O_3 and NiO-$NiAl_{2.54}O_{4.81}$-Al_2O_3 respectively were 4.9×10^{-13} and 3.8×10^{-11} atm respectively. The dissociation pressure of NiO in contact with pure Ni at this temperature was 5.4×10^{-11} atm. A schematic diffusion path is traced on Figure 12. It was constructed assuming that the ratio of Al: Ni in the internal oxidation zone, and the inner layer of the scale, was identical with the bulk alloy. In fact, as discussed below, enrichment of Al in the internal oxidation zone (and presumably the inner scale layer) was evident, together with a corresponding depletion in the alloy immediately ahead of the precipitation front. However, this would not qualitatively affect the present argument, which is that in order to satisfy thermodynamic criteria, the composition of the precipitates must abruptly shift from Al_2O_3 in the region of the precipitation front to $NiAl_2O_4$ towards the subscale/scale interface. Furthermore, it is anticipated that the relative $Al_2O_3/NiAl_2O_4$ thickness would increase with Al content, although it must be emphasized that the length of the diffusion path within a particular phase region does not necessarily have any direct relationship with the thickness of the region of that phase or phases in real space.

Before attempting a quantitative analysis, it is essential to first establish the growth mechanism. Depending on the relative diffusivities and solubilities of oxygen and solute metal in the alloy, two limiting cases are possible (13-15): (i) if $N_O^S D_O \gg N_B^\circ D_B$, growth is controlled by oxygen diffusion and (ii) if these quantities are of similar magnitude, both oxygen and solute metal diffusion are rate

controlling. A clear distinction between the two mechanisms is the formation of a metal denuded zone ahead of the reaction front and an equivalent enrichment in the form of oxide within the precipitation zone in the latter case. Although Al depletion was detectable with EPMA, precise determination of the concentration profile was rather difficult because it occurred over a narrow distance. Therefore, identification of the prevailing mechanism was based on a comparison of the observed volume fraction of the precipitates with that calculated from a mass balance using metal and oxide densities assuming no Al diffusion in the alloy and no volume change accompanying internal oxidation. The results of these measurements, which were based on the linear intercept method (16), are shown in Figure 13 along with the calculated values corresponding to $NiAl_2O_4$ or Al_2O_3. These data are also included in Table I. The calculated volume fraction does not depend significantly on the composition of the precipitates. The absence of structural discontinuities at the transition 'boundary' between the two phases (Figure 6 and 7) is consistent with this finding. Comparing the experimental and calculated values for the spinel phase (Figure 13), it is evident that Al enrichment in all alloy compositions had occurred and that the presence of active elements (Ta and Hf) enhanced this process. The latter observation, in addition to the presence of an Al denuded zone in the alloy ahead of the precipitation front, inferred that at this elevated temperature the growth of the precipitates was controlled by oxygen as well as Al diffusion.

According to the classical internal oxidation model, the growth of the precipitates, under limiting case (ii), in the presence of an external scale as a source of oxygen, is described by (17)

$$\left[\xi\frac{(\xi-\xi')}{t}\right]^{1/2} = [k(k-k')]^{1/2} = \frac{\pi^{1/2}\, N_O^S\, D_O}{\nu_{eff}\, N_{Al}^{\circ}\, D_{Al}^{1/2}} \qquad [5]$$

where ξ, ξ' are the instantaneous depth of the internal oxidation zone and the scale/subscale interface relative to the original alloy surface (i.e, the recession of external scale), respectively: k, k' are the parabolic rate constants for the advance of the two interfaces. Note that the atomic ratio of oxygen to Al in the precipitates of the original equation has been changed to ν_{eff} to account for both spinel and Al_2O_3 being formed within the precipitation zone. In essence, ν_{eff} can be regarded as an adjustable parameter with limiting values of 1.5 and 2.0 corresponding to Al_2O_3 and $NiAl_2O_4$, respectively. Its actual value will depend on the relative thickness of the spinel and Al_2O_3 regions in the internal oxidation zone. Indeed, for the similar, but not identical, case where two oxides, e.g., BO_{ν_1} and BO_{ν_2}, can form internally, this functional dependence has been derived (18).

Since no inner spinel containing layer could be identified in the external scale formed on Ni-0.5 Al alloy, k' is assumed to be negligible in this case. For the other alloys, $k' = 0.19 \times 10^{-4}$ cm/sec$^{1/2}$, independent of Al content. Using a value for the concentration-independent interdiffusion coefficient in γ-NiAl (19,20) at this temperature of 1.4×10^{-9} cm^2/sec. and $\nu_{eff} = 2.0$, the oxygen permeability product $N_0^s D_0$ was calculated from Equation (5). Values are given in Table I, where it is evident that the oxygen permeability is virtually independent of Al concentration, or the presence of the reactive elements. Values range from $0.9\text{-}1.8 \times 10^{-10}$ cm^2/sec. It should be emphasized that the relative amount of the $Al_2O_3/NiAl_2O_4$ phases has no significant bearing on the precipitate growth rate or the calculated oxygen permeability values. This finding is in contrast to the behavior of alloys at lower temperatures, where a strong dependence of the "apparent" $N_0^s D_0$ product on alloy Al content was found (7). Values for a range of alloy compositions, oxidized in 1 atm. oxygen, are shown in Figure 14, where

it is clear that the difference between the various alloy contents diminished with increasing temperature. Included also in Figure 10 are values of $N_0^s D_0$ in 'pure' nickel obtained by extrapolation of plots of $N_0^s D_0$ vs. wt.% Al to 0% Al at the various temperatures (7), and values from independently measured solubilities (21) and diffusivity (22), although this latter work is rather dated. The present datum point for 1200°C fits closely with the extrapolated line through the low temperature oxidation data.

The model advanced for the dependence of the permeability product on alloy Al content considered the contribution of the oxide precipitate/matrix interface in providing enhanced oxygen diffusivities, with the densities of these boundaries increasing with Al content, although this was not measured directly. In the present work, the apparent precipitate/alloy interfacial boundary density can be calculated using the measured distributions. For the three alloy compositions considered, the ratio of these quantities is given by

$$\left[\frac{4\ A_f}{d}\right]_{\text{Ni-2 Al}} : \left[\frac{4\ A_f}{d}\right]_{\text{Ni-4 Al}} : \left[\frac{2\ A_f(W+L)}{W \times L}\right]_{\text{Ni-2 Al-1 Ta}} \qquad [6]$$

which upon substituting the appropriate values from Table I becomes

$$[2.5]_{\text{Ni-2Al}} : [1]_{\text{Ni-4Al}} : [5]_{\text{Ni-2Al-1Ta}} \qquad [7]$$

This relatively small variation in boundary density in contrast to a remarkable difference in precipitate distribution, which arose from varying alloy composition and active element addition, stem from opposing factors namely, alteration of particle shape, size and volume fraction. For instance, increasing the Al content or addition of active element led to an increase in precipitate volume fraction; however, the boundary density per particle was reduced due to increased particle size. Nevertheless, it is believed

that the true boundary density would be significantly different since the boundary width depends on the degree of incoherency, and thence on particle size and shape.

In this latter context, it seems appropriate to consider briefly the factors involved. For other than the 0.5% Al alloy, the internal precipitates always adopted the form of continuous rods or plates extending virtually completely right the way through the internal oxide zone. The reason for this is presumably related to the degree of supersaturation existing ahead of the precipitate zone. It was suggested (24) that oxygen diffuses ahead of the precipitate zone causing the concentration product $N_B\ N_0^{\nu}$ to exceed its equilibrium value at a finite distance ahead of the precipation front. Eventually, it becomes high enough to provide sufficient driving force to nucleate a new oxide particle. There were not sufficient data to carry out similar calculations in the present system, and it can only be assumed that because of the high stability of Al_2O_3 there is never sufficient oxygen diffusing ahead of the precipitation zone to produce significant supersaturation of the matrix with respect to oxide.

Thus, in conclusion, the virtual non dependence of the oxygen permeability on alloy composition, albeit of a variation in interfacial boundary density, inferred that the latter did not enhance oxygen diffusion at high temperatures. The transition to an oxygen diffusion controlling mechanism at lower temperatures (7) was probably associated with a much finer and higher precipitate density.

ACKNOWLEDGEMENTS

This work was supported by the Director, Office of Energy Research, Office of Basic Energy Science, Materials Science Division of the U.S.

Department of Energy under Contract No. DE-AC03-76SF00098. Discussions with Professor W. W. Smeltzer, McMaster University were especially helpful.

TABLE I

Experimental and Calculated Data for the Internal Oxidation of Ni-Al Alloys

Alloy Composition	N_{Al}	$k \times 10^4$ cm/sec$^{1/2}$	$\bar{d}$ μm	$\bar{S}$ μm	V_f or A_f calculated Al_2O_3	calculated $Ni_2Al_2O_4$	measured	$N_0^S D_0 \times 10^{10}$ cm^2/sec
Ni-0.5Al	0.011	1.94	-	-	0.02	0.032	0.14	0.9
Ni-2Al	0.043	0.83	1.26±0.04	3.3±0.12	0.08	0.12	0.27	1.3
Ni-4Al	0.083	0.61	4.15±0.1	6.6±0.25	0.155	0.24	0.35	1.8
Ni-2Al-1Ta	0.043	1.04	L=5.5± 0.3 W=0.5± .01	-	-	-	0.36	1.8
Ni-2Al-1Hf	0.043	1.04	-	-	-	-	0.40	1.8

N_{Al}:- Al atom fraction, k: precipitate growth rate constant, $\bar{d}$: average particle size

L: side length, W: width, $\bar{S}$: average particle spacing, V_f: volume fraction

A_f: fractional surface coverage.

FIGURE CAPTIONS

Figure 1. Internal oxide morphology at the vicinity of alloy grain boundaries illustrating uniform penetration and denser oxide population. (a) and (b) Ni-2Al-1Ta, (c) Ni-2Al-1Hf, (d) and (e) microstructure of grain boundary precipitates in the Ni-0.5 Al alloy.

Figure 2. Internal oxide morphology in the Ni-0.5 Al alloy. (a) cross section, (b) transverse section at a triple grain boundary intersection, (c) polyhedral crystallites at the outer internal oxidation zone, (d) sporadically distributed spherical and oriented platelets in the inner region.

Figure 3. Internal oxide morphology in the Ni-4Al alloy. (a) and (b) longitudinal and transverse sections across the cylindrical rod-like precipitates, respectively, (c) and (d) similar sections illustrating the development of a continuous Al_2O_3 film at the precipitation front.

Figure 4. Internal oxide morphology in the Ni-2Al-1Ta alloy. (a) cross section, (b) structural details in the vicinity of alloy grain boundary precipitates, (c) and (d) transverse sections across depicting a plate-like morphology.

Figure 5. Internal oxide morphology in the Ni-2Al-1Hf alloy (a) cross section, (b) close-up view of the precipitates.

Figure 6. Ni and Al x-ray maps of the rod like precipitates in the Ni-4Al alloy.

Figure 7. Hf, Ni and Al x-ray maps of the precipitation zone in the Ni-2Al-1Hf alloy.

Figure 8. Over-all scale morphology on the Ni-2Al-1Ta alloy.

Figure 9. Parabolic plot of internal oxide growth.

Figure 10. Precipitate size and spacing distributions.

Figure 11. Transverse sections through the internal oxidation zone.

Figure 12. Ni-rich region of the Ni-Al-O phase diagram at 1000°C, including a schematic diffusion path.

Figure 13. Volume fraction of oxide precipitates as a function of Al content.

Figure 14. Arrhenius plot of the oxygen permeability product in γ-NiAl solid solution alloys.

REFERENCES

1. J. S. Wolf and E. B. Evans, Corros.-NACE, 18, 129t (1962).

2. W. C. Hagel, Corros., 21, 316 (1965).

3. F. S. Pettit, Trans. Met. Soc. AIME, 239, 1296 (1967).

4. F. H. Stott and G. C. Wood, Corros. Sci., 17, 647 (1977).

5. H. Hindam and W. W. Smeltzer, J. Electrochem. Soc., 127, 1622 (1980).

6. W. W. Smeltzer, H. Hindam and F. A. Elrefaie, Proceedings of the NACE Conference on High Temperature Corrosion, San Diego, California (1981).

7. D. P. Whittle, Y. Shida, G. C. Wood, F. H. Stott and B. D. Bastow, Philosophical Magazine A, in press.

8. F. A. Elrefaie and W. W. Smeltzer, submitted to Oxid. of Metals (preprint furnished by author).

9. F. A. Elrefaie and W. W. Smeltzer, J. Electrochem. Soc., 128, 2237 (1981).

10. H. Hindam, Ph.D. Thesis: 'Microstructure and Growth of Al_2O_3 on Ni-Al Alloys', McMaster University (1979).

11. JANAF Thermochemical Tables, 2nd Ed. (1971).

12. R. Hultgren, P. D. Desai, D. T. Hawkins, M. Gleiser and K. K. Kelly, 'Selected Values of the Thermodynamic Properties of Binary Alloys', p. 191, Amer. Soc. Met., Metals Park, Ohio (1973).

13. C. Wagner, Z. Elektrochem., 63, 772 (1959).

14. R. A. Rapp, Corrosion, 21, 382 (1965).

15. J. H. Swisher, 'Oxidation of Metals and Alloys', Ed. D. L. Douglass, p. 235, Amer. Soc. Met. (1971).

16. E. E. Underwood, 'Metals Handbook', vol. 8, 8th Ed., Ed. T. Lyman, Amer. Soc. Met. (1973).

17. F. Maak, Z. Metallkunde, 52, 545 (1961).

18. T. L. Meijering, 'Adv. in Mat. Res.,' Ed. H. Herman, 5, 1 (1971).

19. J. D. Whittenberger, Met. Trans., 3, 2010 (1972).

20. M. M. P. Janssen, ibid, 4, 1623 (1973).

21. A. V. Seybolt, quoted in 'Metals Ref. Handbook', Ed. C. J. Smithells, 5th Ed., Butterworths (1976).

22. C. J. Smithells and C. E. Ransley, Proc. Roy. Soc., A155, 195 (1936).

23. G. Böhm and M. Kahlweit, Acta Met., 12, 641 (1964).

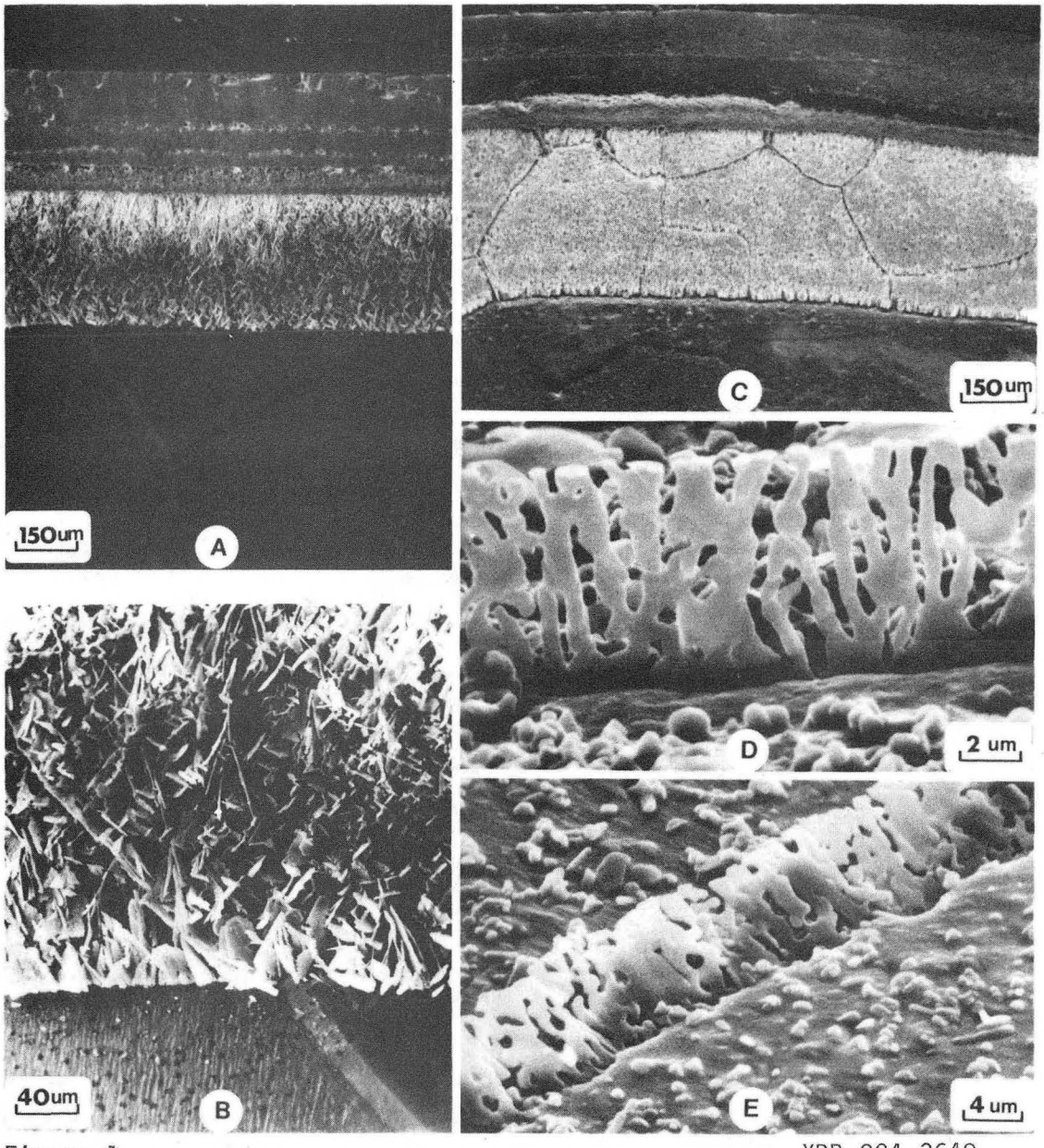

Figure 1.

XBB 824-3648

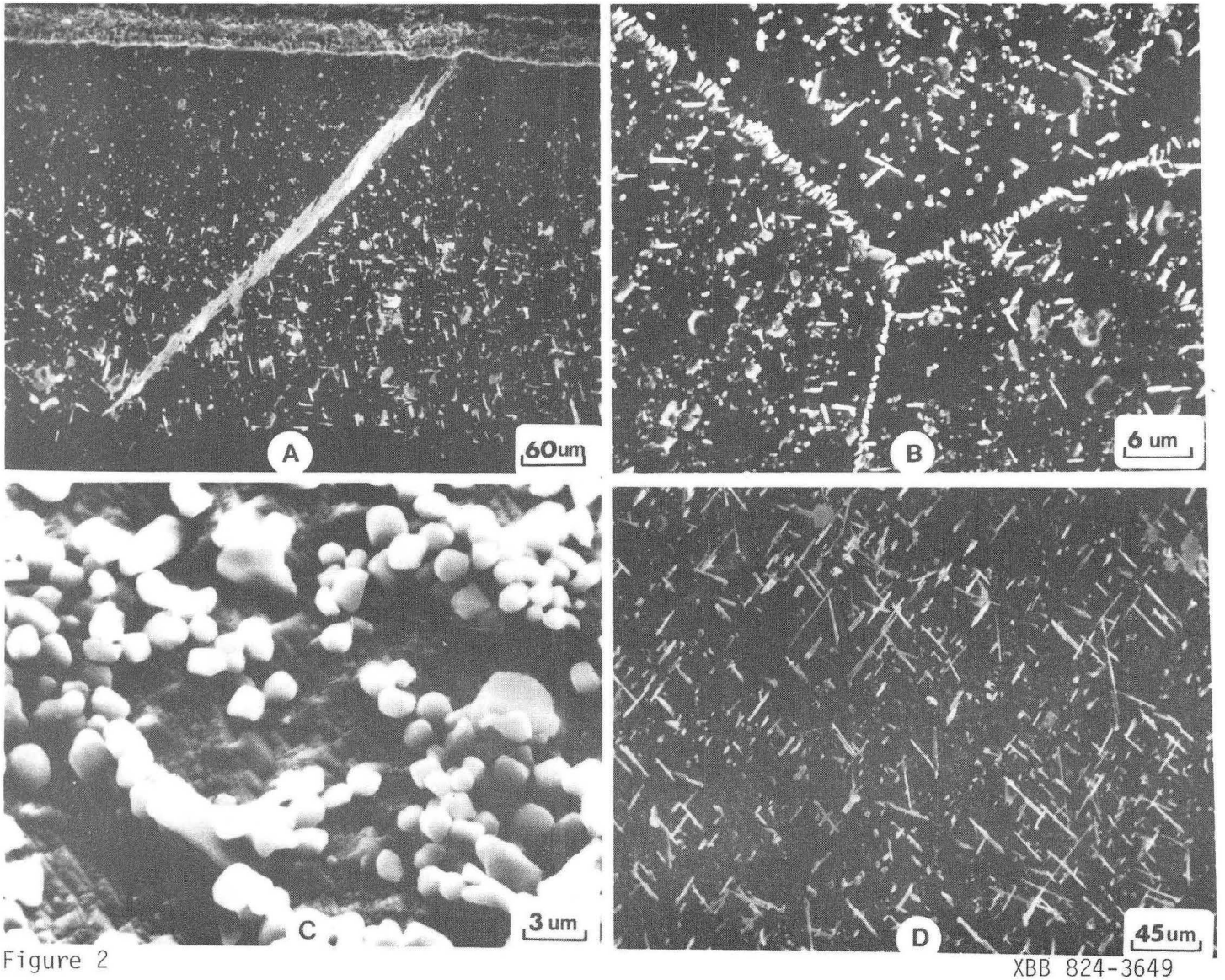

Figure 2

XBB 824-3649

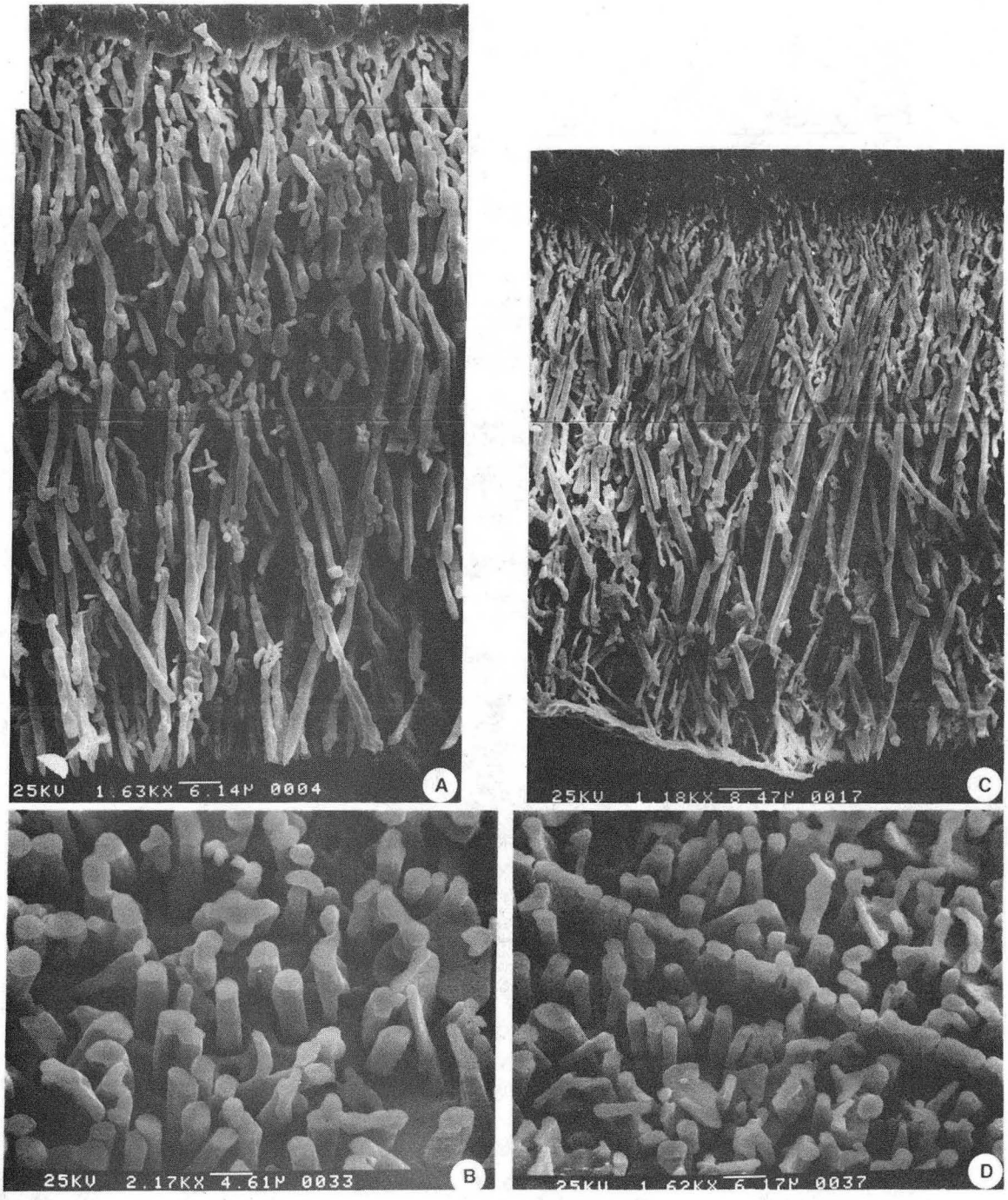

Figure 3.

XBB 824-3654

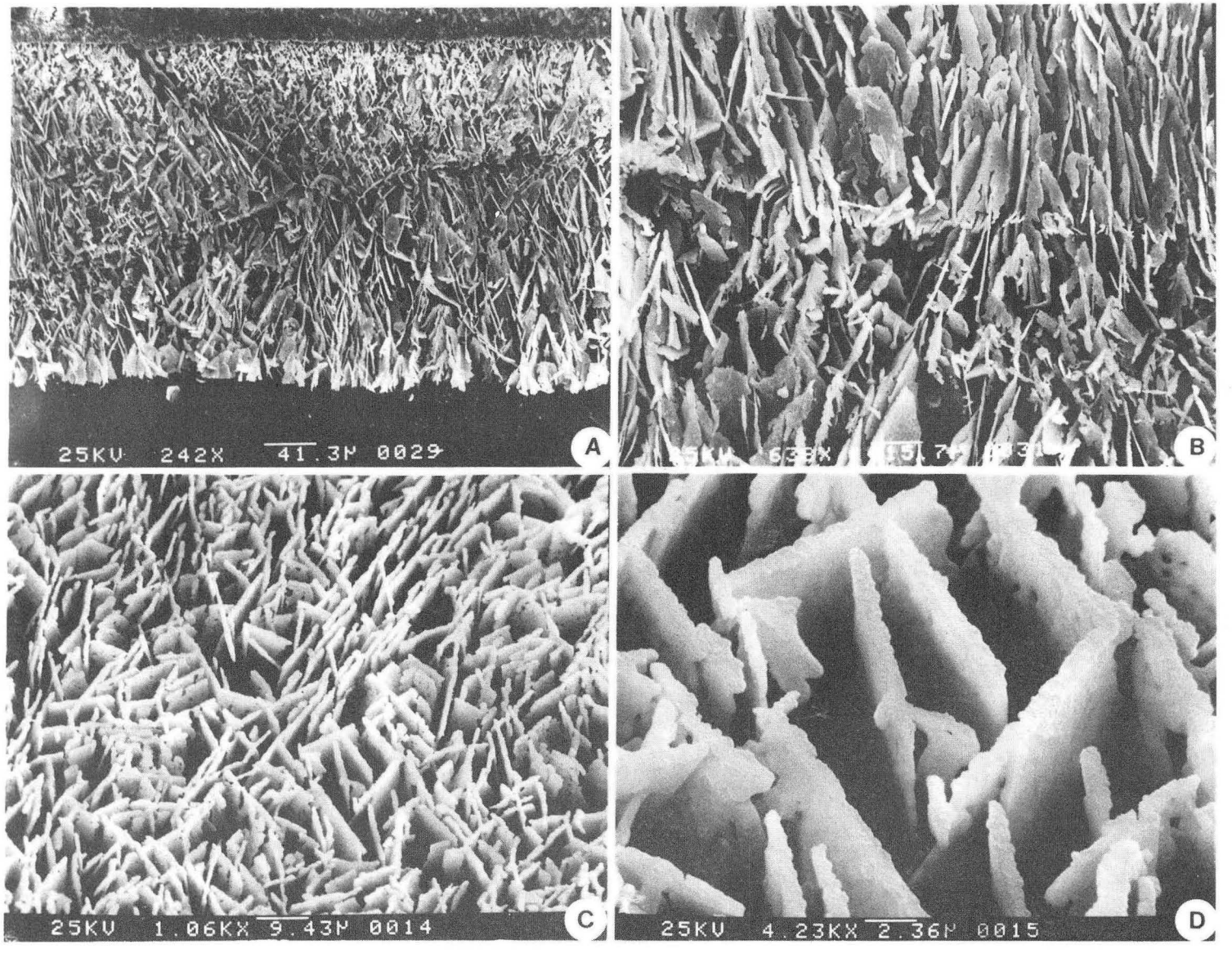

Figure 4

XBB 824-3653

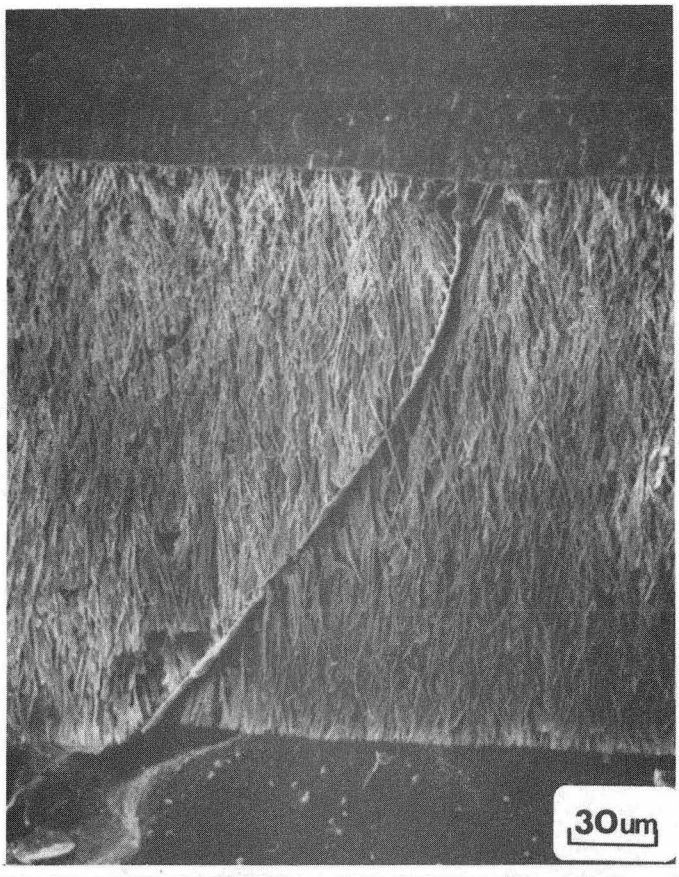

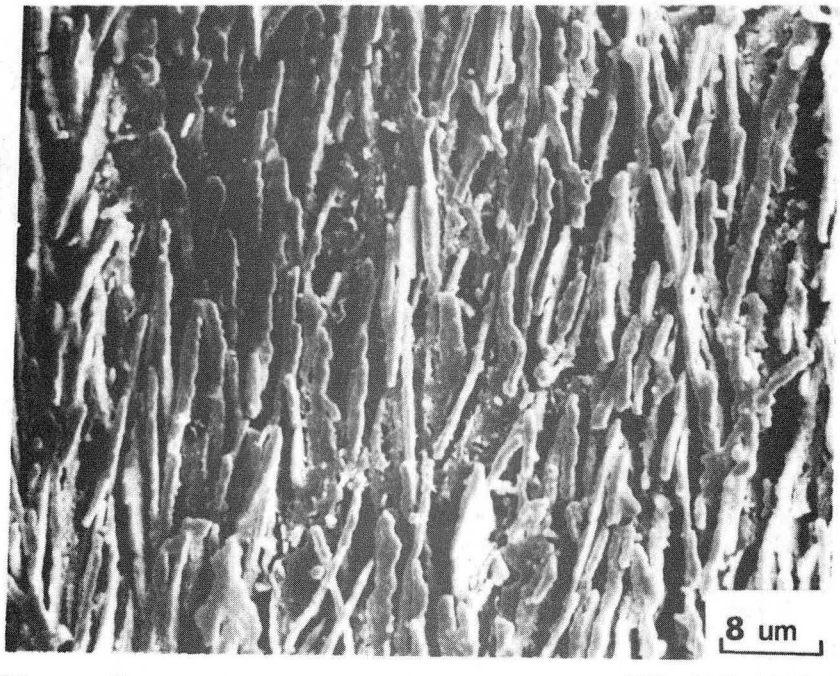

Figure 5 XBB 824-3651

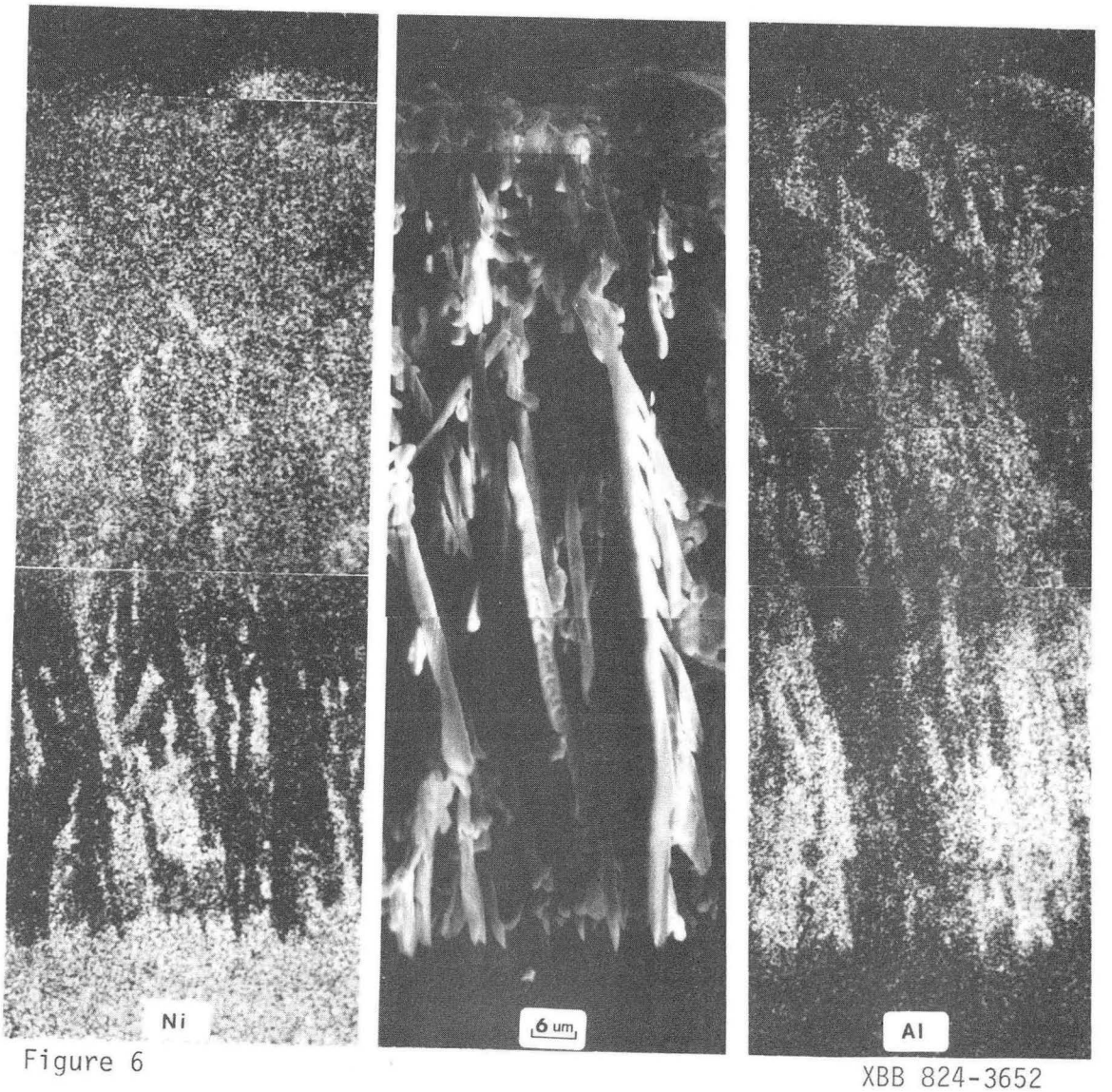

Figure 6

XBB 824-3652

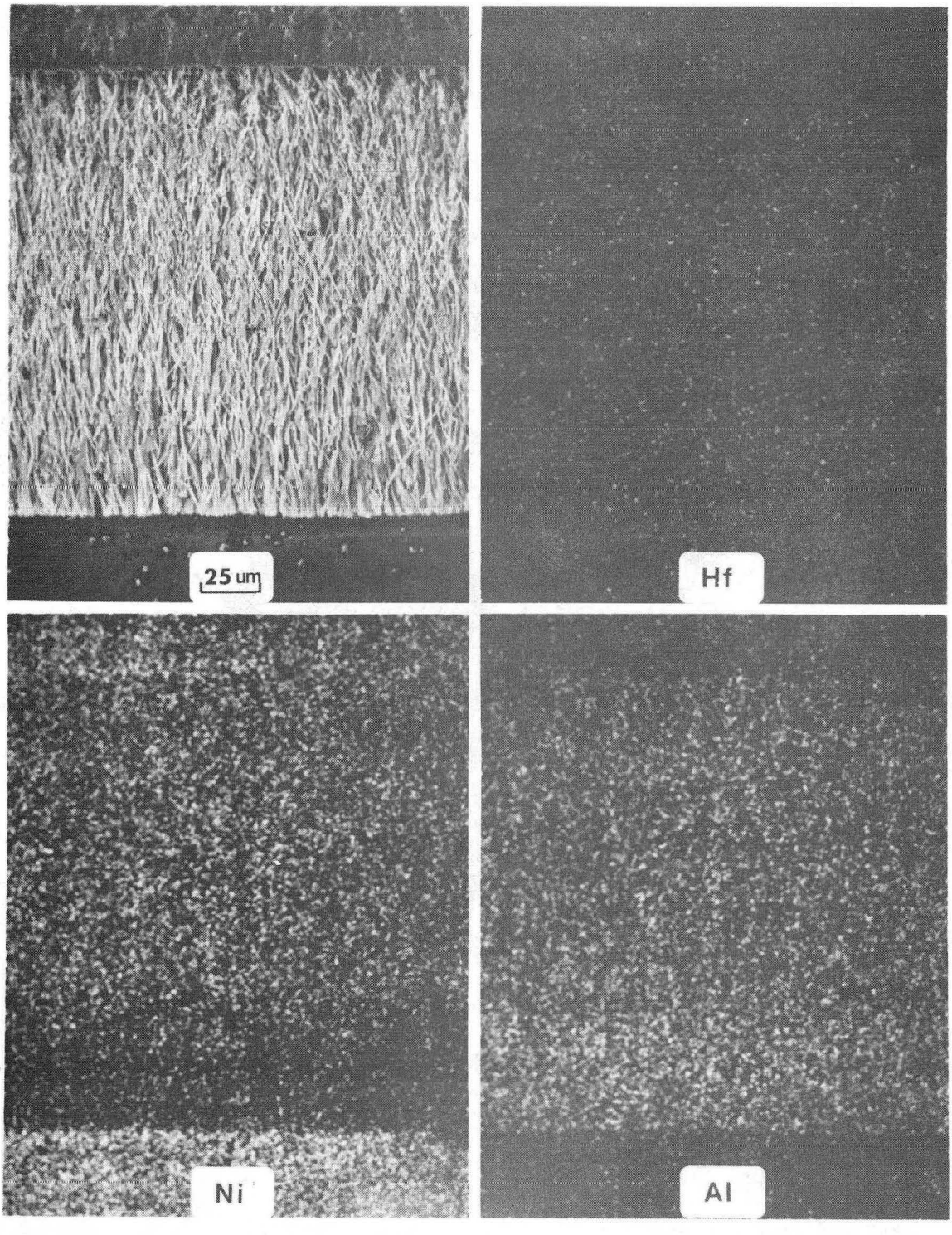

Figure 7

XBB 824-3650

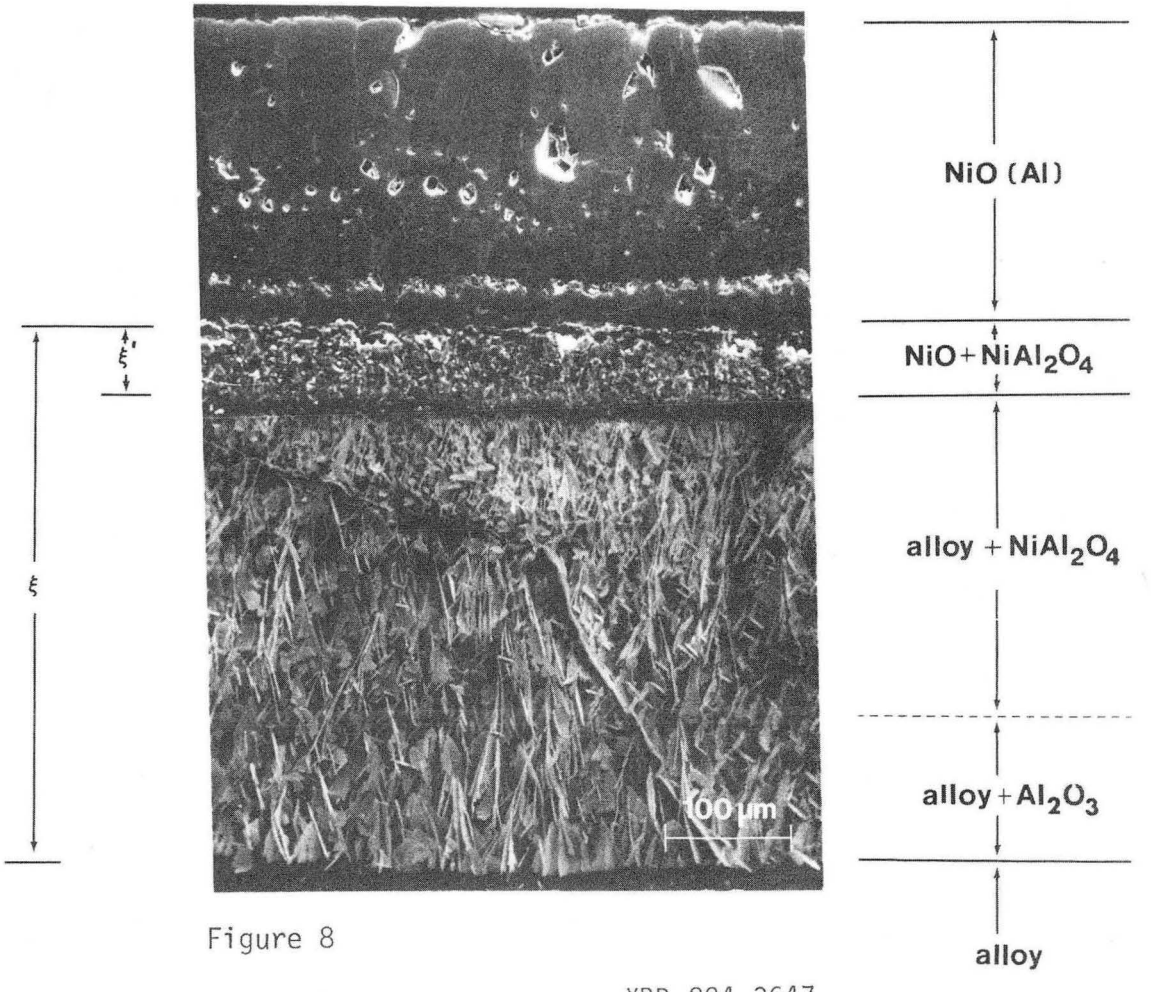

Figure 8

XBB 824-3647

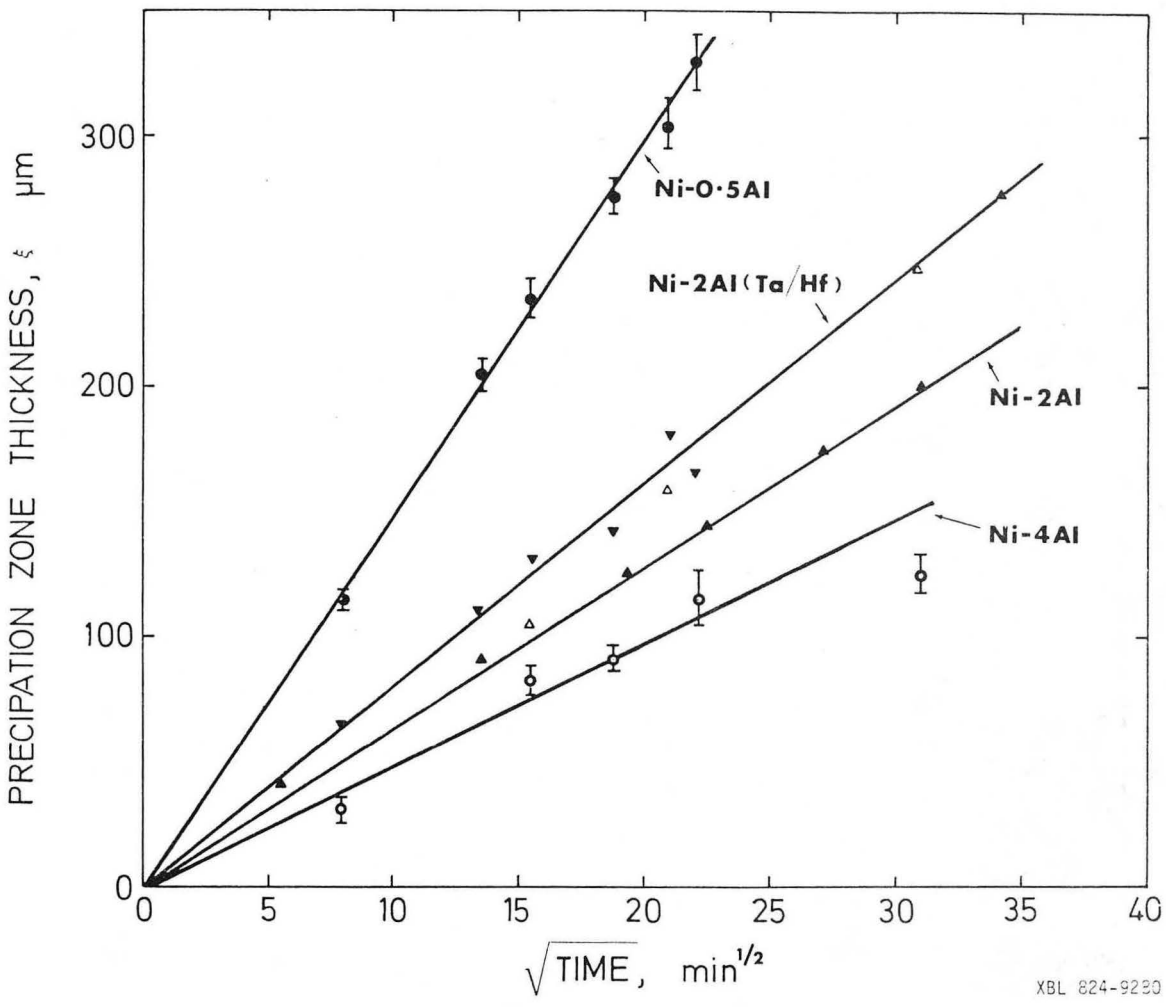
PRECIPATION ZONE THICKNESS, ξ μm
300
200
100
0
0
5
10
15
20
25
30
35
40
√TIME, min^1/2
Ni-0·5Al
Ni-2Al(Ta/Hf)
Ni-2Al
Ni-4Al
XBL 824-9230

Figure 9

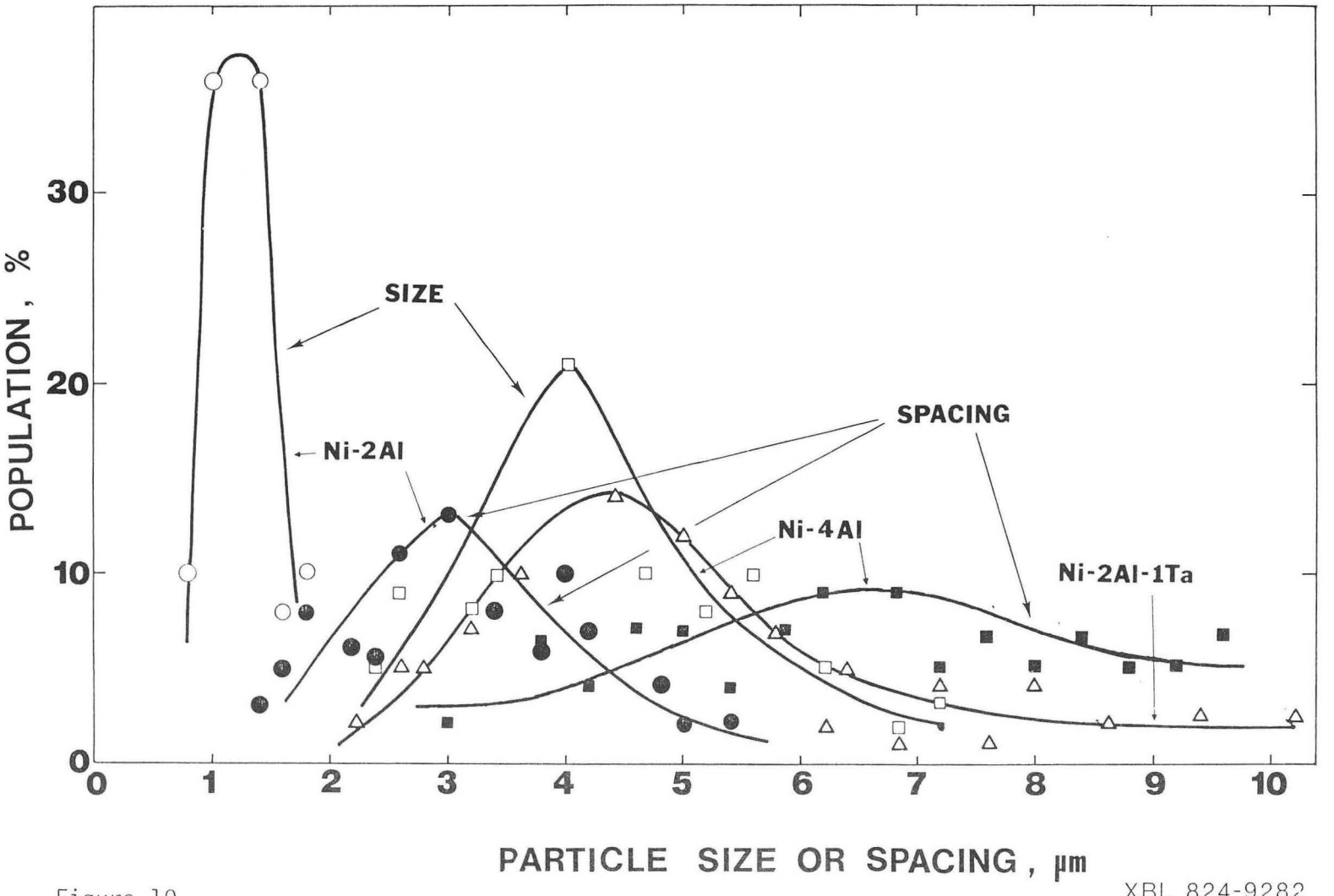

Figure 10

XBL 824-9282

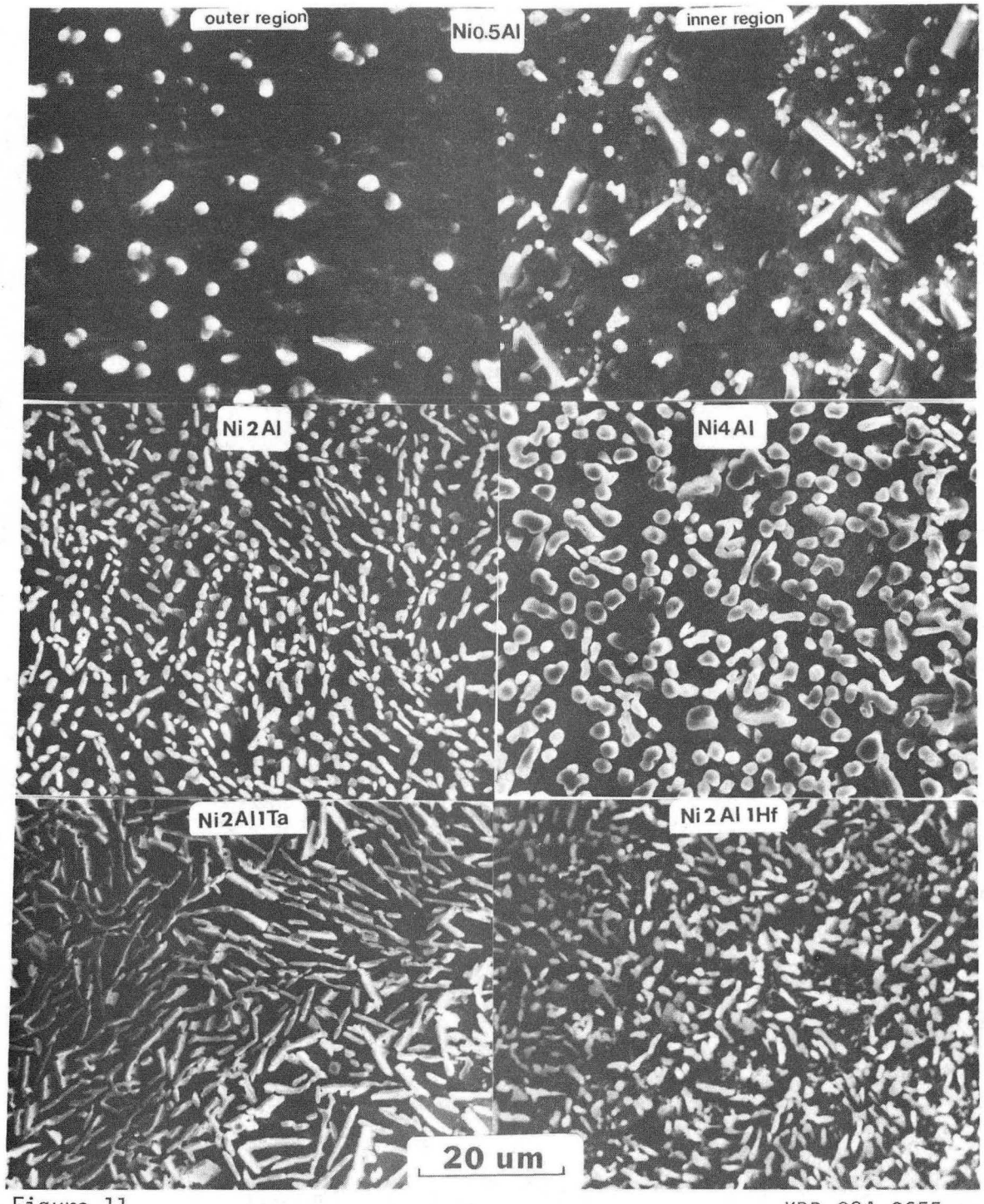

Figure 11

XBB 824-3655

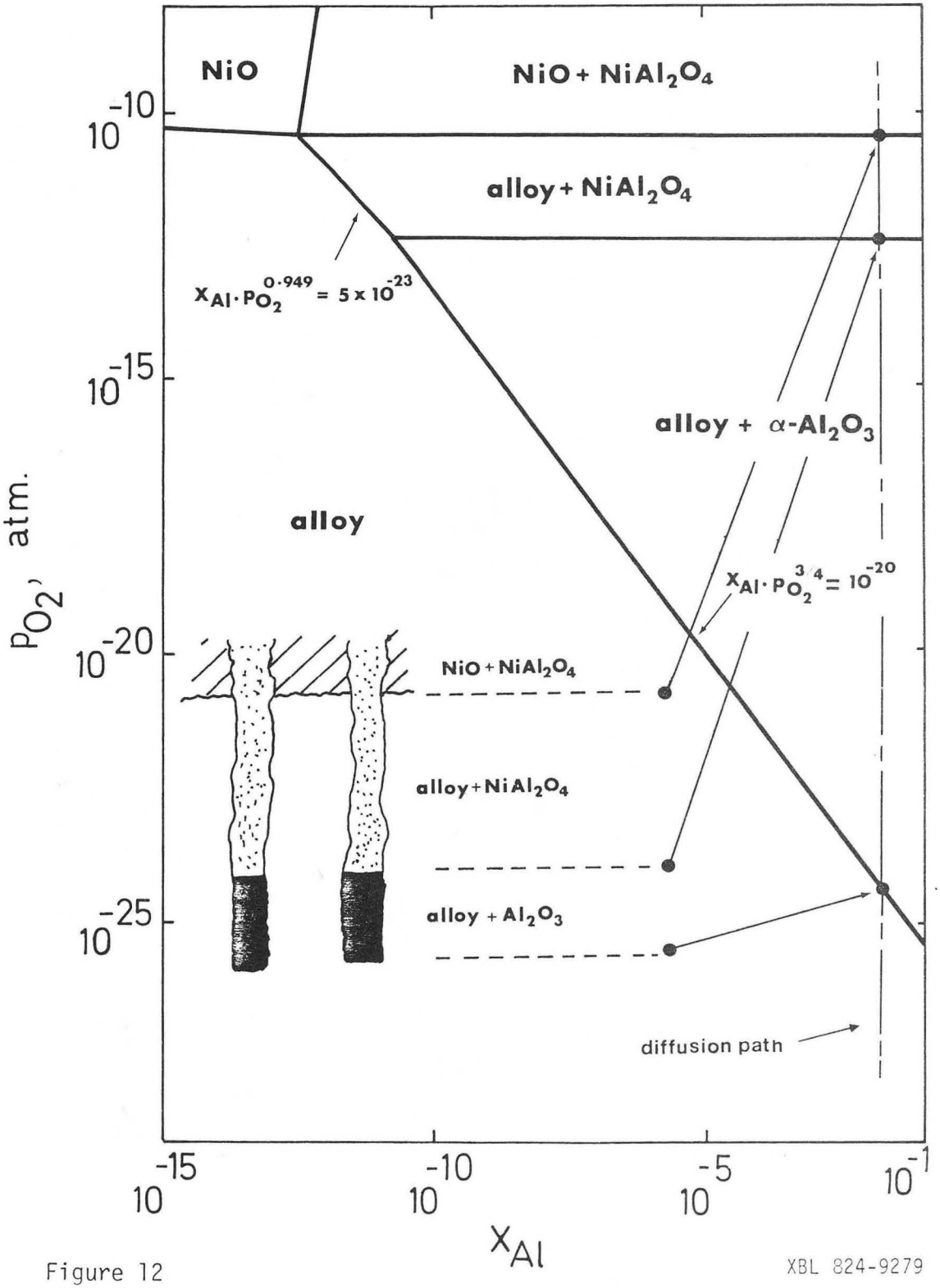

Figure 12

XBL 824-9279

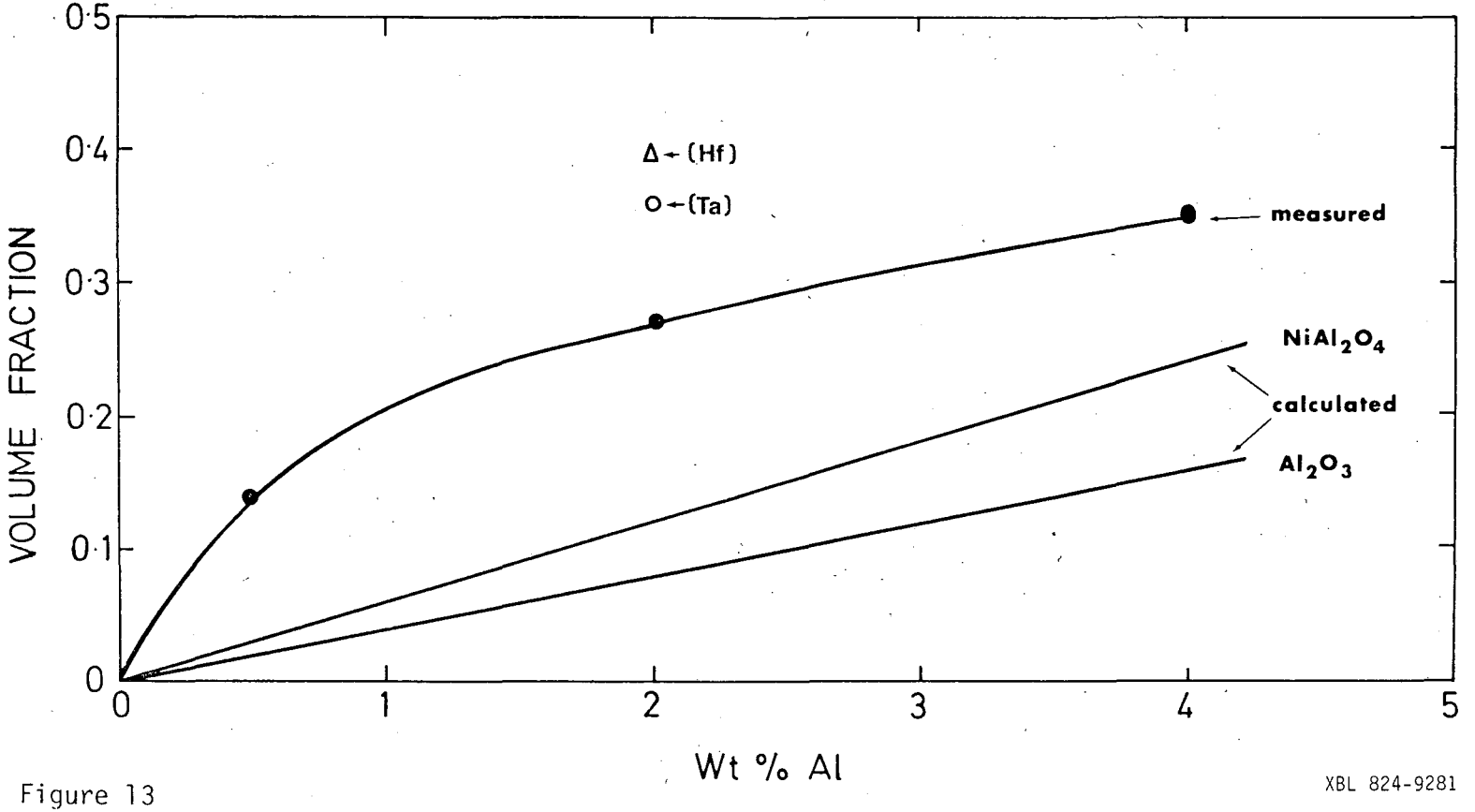

Figure 13

XBL 824-9281

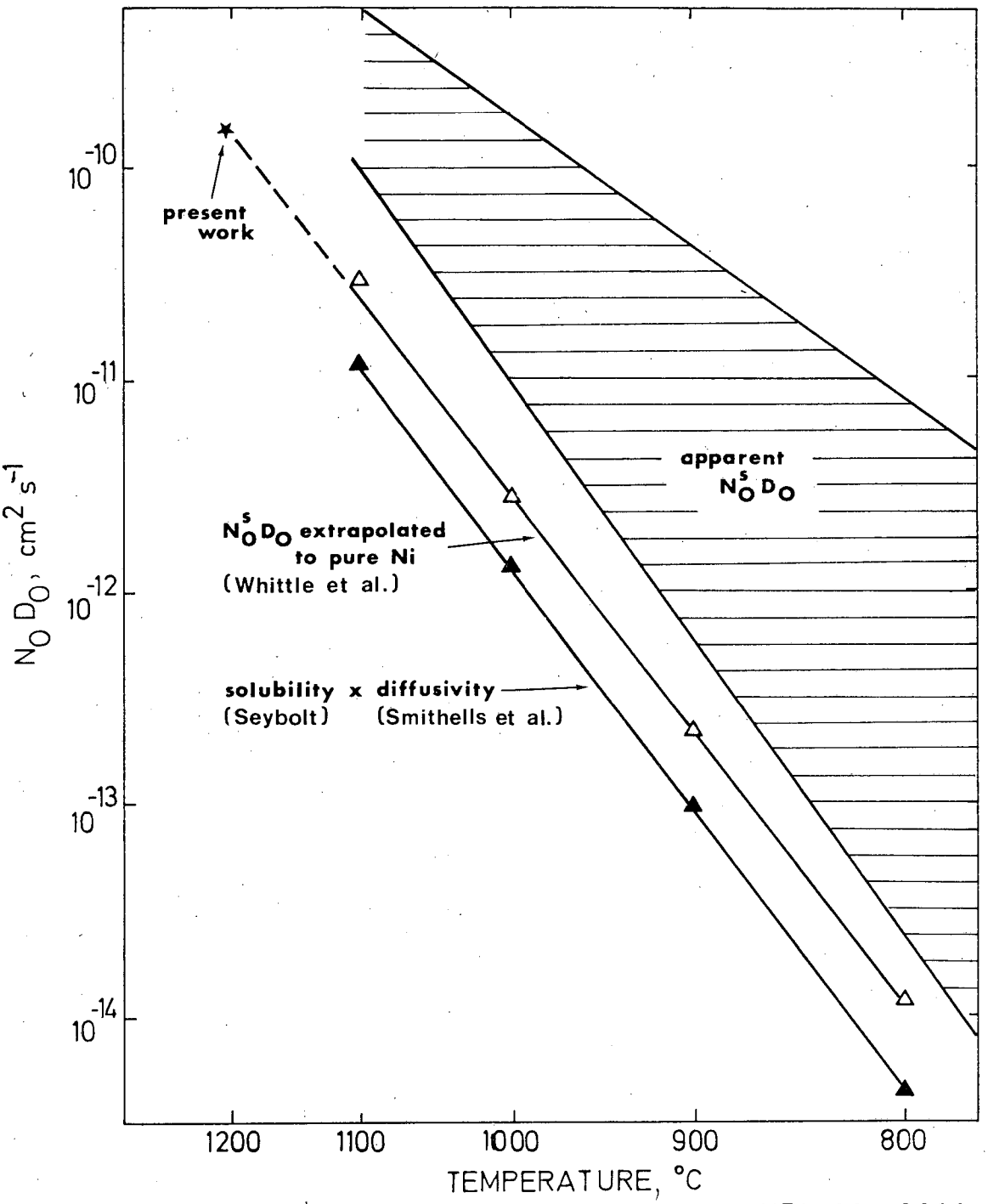

Figure 14

XBL 824-9283

TECHNICAL INFORMATION DEPARTMENT
LAWRENCE BERKELEY LABORATORY
UNIVERSITY OF CALIFORNIA
BERKELEY, CALIFORNIA 94720